

Nanoengineering Liquid Metal Core–Shell Nanostructures

Hongda Lu, Shi-Yang Tang,* Jiayuan Zhu, Xumin Huang, Helen Forgham, Xiangke Li, Ao Shen, Guolin Yun, Jinming Hu, Shiwu Zhang, Thomas P. Davis, Weihua Li,* and Ruirui Qiao*

Nanoengineering the composition and morphology of functional nanoparticles endows them to perform multiple tasks and functions. An intriguing strategy for creating multifunctional nanomaterials involves the construction of core–shell nanostructures, which have enabled promising applications in biomedicine, energy, sensing, and catalysis. Here, a straightforward nanoengineering approach is presented utilizing liquid metal nanoparticles and galvanic replacement to create diverse core–shell nanostructures. Controlled nanostructures including liquid metal core–gold nanoparticle shell (LM@Au), gold nanoparticle core–gallium oxide shell (Au@Ga oxide), and hollow Ga oxide nanoparticles are successfully fabricated. Remarkably, these investigations reveal that LM@Au exhibits exceptional photothermal performance, achieving an impressive conversion efficiency of 65.9%, which is five times that of gold nanoparticles. By leveraging the high photothermal conversion efficiency and excellent biocompatibility of LM@Au, its promising application in hyperthermia cancer therapy is demonstrated. This simple yet powerful nanoengineering strategy opens new avenues for the controlled synthesis of complex core–shell nanostructures, advancing various fields beyond biomedicine.

structures.^[1] To obtain tailored functionalities, multifarious nanostructures such as nanocubes, nanowires, and nanocages have been designed and fabricated.^[2] One intriguing class of nanostructures is the core–shell configuration, analogous to a pearl composed of a central core surrounded by distinct layers of nacre.^[3] Such core–shell nanostructures offer tremendous opportunities for tailoring material properties and have shown promise in various applications such as imaging,^[4] drug delivery,^[5] and photonic catalysis.^[6]

For solid materials, fabrication methods including chemical polymerization, self-assembly, sol–gel, and coprecipitation have been developed over decades to fulfill the coating of desired polymers, proteins, and nanoparticles (NPs) on the core surface.^[7] Notably, the galvanic replacement has been explored for creating complex nanostructures with tailored compositions and morphologies.^[8] The facile technique allows the replication of the mor-

phology and structure of the sacrificial template, while simultaneously introducing a different metal or metal compound. Unlike solid metals, core–shell nanostructures of liquid metal (LM) materials are often overlooked. One of the widely explored liquid

1. Introduction

Nanoengineering harnesses the power of manipulating matter at the nanoscale, enabling control over material properties and

H. Lu, W. Li
School of Mechanical, Materials, Mechatronic and Biomedical Engineering
University of Wollongong
Wollongong, NSW 2522, Australia
E-mail: weihuali@uow.edu.au


S.-Y. Tang
School of Electronics and Computer Science
University of Southampton
Southampton SO17 1BJ, UK
E-mail: shiyang.tang@soton.ac.uk

J. Zhu, X. Huang, H. Forgham, X. Li, A. Shen, T. P. Davis, R. Qiao
Australian Institute for Bioengineering and Nanotechnology
The University of Queensland
St Lucia, QLD 4072, Australia
E-mail: r.qiao@uq.edu.au

G. Yun
Department of Engineering
University of Cambridge
The Old Schools, Trinity Ln, Cambridge CB2 1TN, UK

J. Hu
Department of Pharmacy
The First Affiliated Hospital of USTC
Division of Life Sciences and Medicine
Department of Polymer Science and Engineering
University of Science and Technology of China
96 Jinzhai Road, Hefei, Anhui Province 230026, China

S. Zhang
CAS Key Laboratory of Mechanical Behavior and Design of Materials
Department of Precision Machinery and Precision Instrumentation
University of Science and Technology of China
Hefei 230026, China

 The ORCID identification number(s) for the author(s) of this article can be found under <https://doi.org/10.1002/adfm.202311300>

© 2023 The Authors. Advanced Functional Materials published by Wiley-VCH GmbH. This is an open access article under the terms of the Creative Commons Attribution License, which permits use, distribution and reproduction in any medium, provided the original work is properly cited.

DOI: 10.1002/adfm.202311300

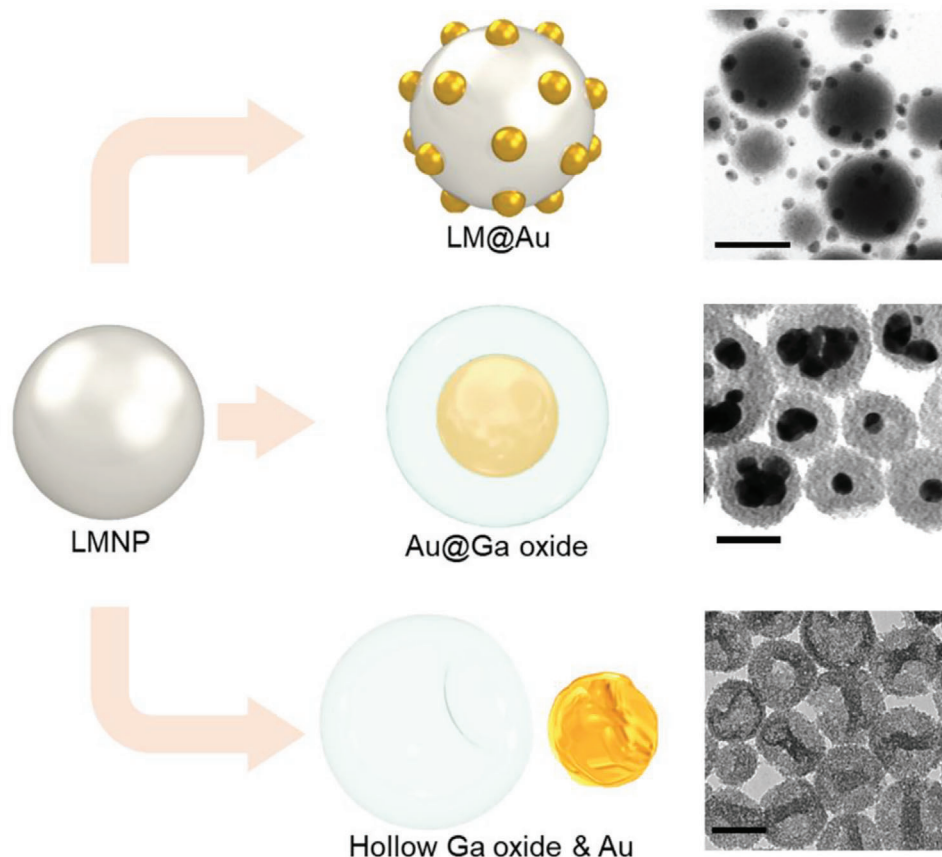


Figure 1. Schematic and representative transmission electron microscopy images illustrating the tunable core-shell nanostructures enabled by galvanic replacement of LMNPs. Scale bars are 100 nm.

functional materials in recent years is gallium-based LMs, such as eutectic gallium-indium (EGaIn) and eutectic gallium-indium-tin (Galinstan). NPs made of these LMs exhibit promising biomedical applications, due to their distinctive attributes, such as stimuli-responsive characteristics, near-indefinite deformability, relatively good biocompatibility, anti-inflammatory or antimicrobial functionalities, tunable morphologies, and superior thermal and electrical conductivities.^[9] Liquid metal nanoparticles (LMNPs) can be readily produced from bulk materials by applying mechanical shear forces (e.g., sonication and high-speed rotation), and the quick formation of a solid oxide layer on the surface prevents coalescence.^[10] Polymer coating of the LMNP surface enhances chemical and colloidal stability and can lead to further surface functionalization.^[9c,11]

The galvanic replacement has been utilized to create LM core-solid metal NP shell structures, incorporating metals such as silver, gold, platinum, and copper.^[12] These structures combine the synergistic properties of the LM core and solid metal NP shell, enabling diverse applications such as photocatalysis,^[13] self-healing flexible circuits,^[14] photothermal therapy,^[15] and magnetic resonance imaging.^[16] However, the conventional core-shell structures generated through galvanic replacement have random NP shells with uncertain size distribution and morphology.^[17] This lack of control hinders the understanding of how to precisely tune the properties of core-shell nanostructures using galvanic

replacement. Moreover, the chemical and colloidal stability of LM core-shell nanostructures remains unexplored, limiting their potential applications, particularly in the biomedical field.

In this study, we present a straightforward nanoengineering approach utilizing LMNPs and galvanic replacement to create diverse core-shell nanostructures. Specifically, we demonstrate the fabrication of LM core-gold NP shell (LM@Au), gold core-gallium oxide shell (Au@Ga oxide), and hollow Ga oxide shell with separated gold nanoparticles (AuNPs), as depicted in **Figure 1**. We co-sonicate bulk EGaIn within the brushed poly(ethylene glycol) methyl ether methacrylate (PEGMA) polymer solution to produce PEG-grafted LMNPs with excellent colloidal stability. By introducing chloroauric acid (HAuCl_4) and hexadecyltrimethylammonium bromide (CTAB) to the LMNPs solution, we fabricate LM@Au nanostructures with evenly distributed, similarly sized AuNPs coating. Notably, by adjusting the chemical concentration and the sequence of addition, we discover the formation of unprecedented Au@Ga oxide and hollow Ga oxide nanostructures. We further discover that the addition of sodium dihydrogen phosphate (NaH_2PO_4) into the NP solution effectively inhibits the growth of the Ga oxide layer in the core-shell nanostructure, enabling precise control of the morphology of the LM@Au nanostructures. More importantly, LM@Au exhibits superior photothermal conversion efficiency, reaching 65.9% under near-infrared (NIR) light, which is twice that of

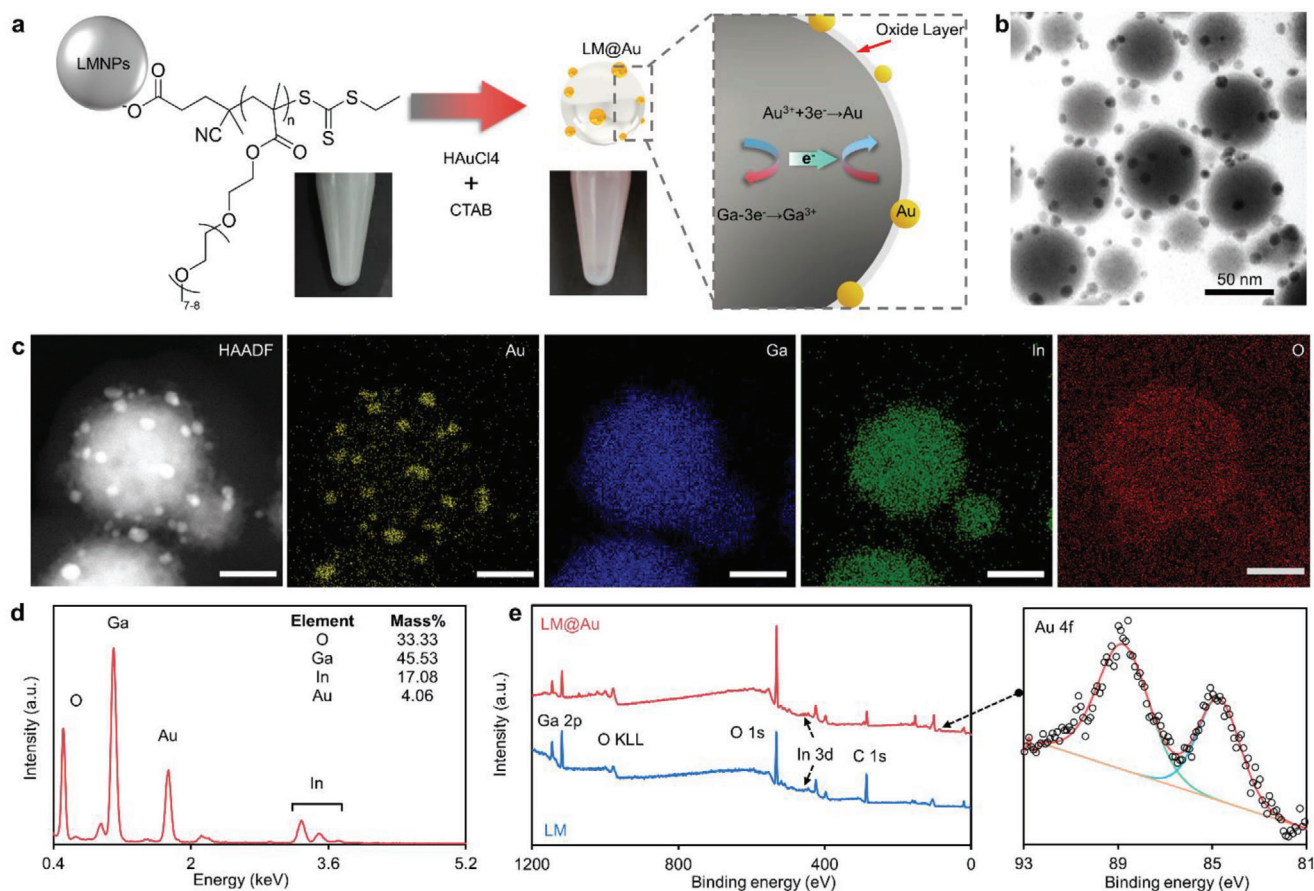


Figure 2. Synthesis and characterization of LM@Au. a) Schematic illustrating the production process of LM@Au. The optical images are LMNPs and LM@Au suspensions respectively. The right inset image illustrates the mechanism of galvanic replacement of LM with AuCl_4^- . b) TEM image of LM@Au. c) HAADF image and EDS elemental maps of Au, Ga, In, and O. Scale bars are 50 nm. d) EDS spectrum of LM@Au. e) XPS survey spectra of LM@Au and LMNPs. A high-resolution XPS spectrum for Au 4f is displayed on the right.

LMNPs (34.3%) and ≈ 5 times that of AuNPs (13.2%). Additionally, NaH_2PO_4 -treated LM@Au displays excellent stability in biological buffers over 30 days, retaining its original structure and maintaining high photothermal conversion efficiency. Harnessing the outstanding stability and photothermal conversion efficiency of LM@Au, we explore its potential in photothermal cancer therapy. Our simple and versatile strategy offers a pathway to create tunable core-shell nanostructures with desirable properties, opening up possibilities for a wide range of applications.

2. LM@Au Synthesis and Characterization

We employed PEGMA (see Figures S1 and S2, Supporting Information, for details) to graft LMNPs due to its capability of preventing LMNPs from aggregation and precipitation.^[18] Briefly, we added PEGMA solution (4 mg mL^{-1}) and EGaln (200 mg) into a glass vial and then used a sonication probe with a temperature control system^[19] to produce LMNPs (Figure 2a). By varying the centrifugation speed to eliminate larger particles, LMNPs with different hydrodynamic sizes and gallium (Ga) concentrations were obtained (see Figure S3a,b, Supporting Information). The obtained LMNP suspension was then mixed with CTAB (final concentration of 20 mM) and HAuCl_4 (final concentration of

100 μM). The color of the solution changed from grey to coral red in a few minutes, indicating the formation of AuNPs. The transformation of AuCl_4^- to AuNPs occurred through galvanic replacement, facilitated by the electrons provided by Ga inside the LMNPs. The transmission electron microscopy (TEM) image (Figure 2b) confirms the formation of LM@Au nanostructures with a uniform distribution of AuNPs on the surface of the LMNPs. To further analyze the composition and distribution of elements, high-angle annular dark field (HAADF) imaging and energy-dispersive X-ray spectroscopy (EDS) mappings are performed on a single LM@Au nanostructure (Figure 2c). These images reveal the uniform distribution of Ga and indium (In) inside the LM@Au nanostructure, with a Ga oxide layer covering the surface. Additionally, the AuNPs are observed to attach to the oxide layer, displaying an even size distribution.

The presence of Au in the LM@Au nanostructures is further confirmed by the EDS spectrum (Figure 2d), and the mass ratio of elements indicates that Ga has been utilized to reduce Au. The LM@Au nanostructure is further evidenced by the X-ray photoelectron spectroscopy (XPS) spectra (Figure 2e). Peaks including Ga 2p, In 3d, O 1s, and C 1s are detected for both LMNPs and LM@Au, while the high-resolution spectrum for the Au 4f peak (84.7 and 88.8 eV) is only detected in the LM@Au.

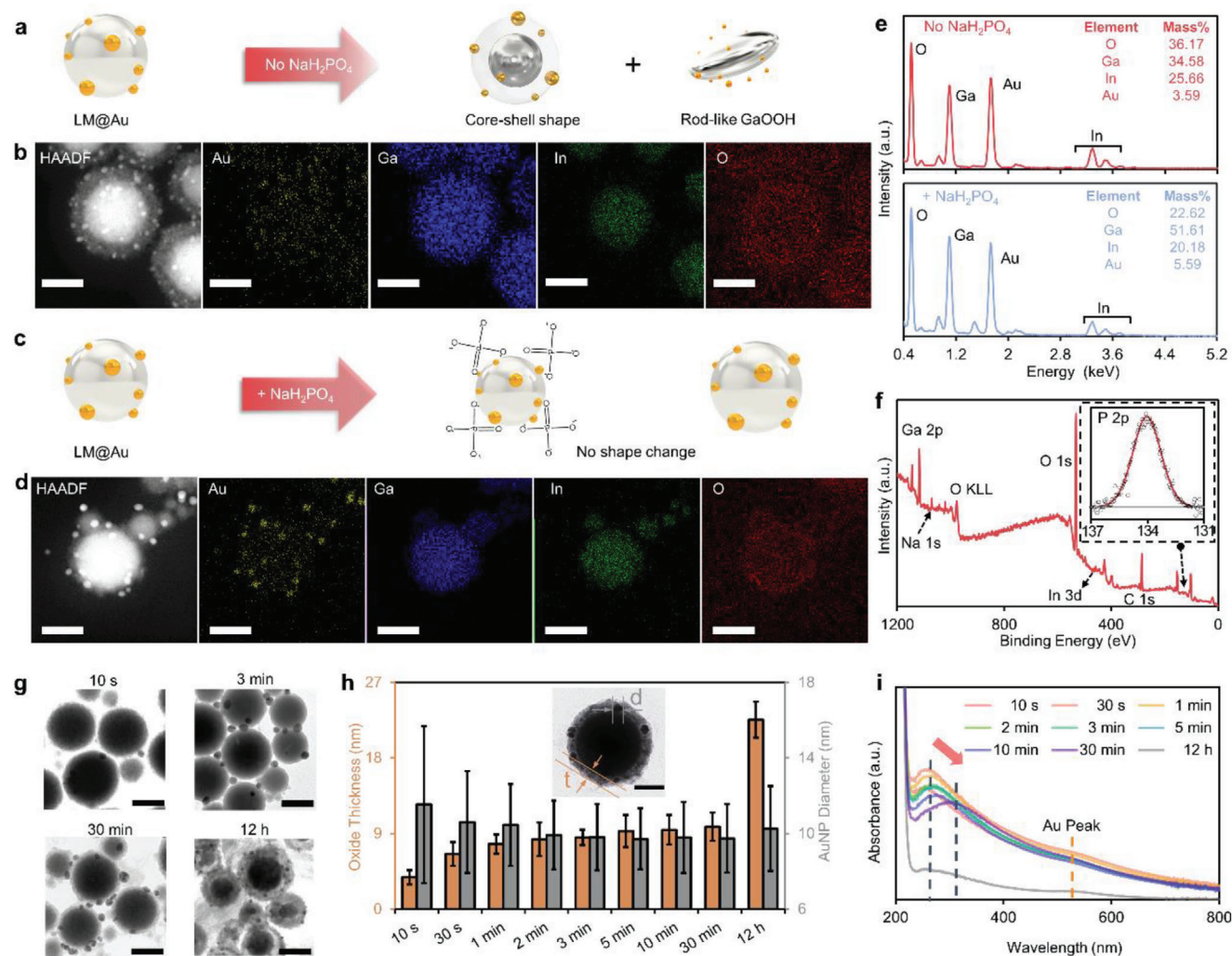


Figure 3. Investigating the influence of phosphate on LM@Au. a) Shape transformation of LM@Au without NaH_2PO_4 . b) HAADF images and EDS elemental maps of Au, Ga, In, and O for untreated LM@Au. c) No shape changes for LM@Au treated with NaH_2PO_4 . d) HAADF images and EDS elemental maps of Au, Ga, In, and O for passivated LM@Au. e) EDS spectra of untreated and treated LM@Au. f) XPS survey spectrum of treated LM@Au. The inset shows the high-resolution XPS spectrum for P 2p signal. g) TEM images of LM@Au with the addition of NaH_2PO_4 at 10 s, 3 min, 30 min, and 12 h after the galvanic reaction. h) Variation of Ga oxide thickness and AuNP diameter and i) UV-vis spectra for LM@Au treated with NaH_2PO_4 at different time points. Scale bars are 50 nm.

In addition, the Au peak for LM@Au displays a positive shift of binding energies compared with pure AuNPs (Figure S4a, Supporting Information), implying the adhesion of Au on the oxide layer. The X-ray diffraction (XRD) spectra for LMNPs and LM@Au (Figure S4b, Supporting Information) further verify the formation of LM@Au. Additionally, Fourier-transform infrared spectroscopy (FTIR) spectra for AuNPs, LMNPs, LM@Au, and PEGMA (Figure S4c, Supporting Information) indicate that AuNPs bind to the surface of LMNPs.

3. Optimization of LM@Au Nanostructures

Upon storing LM@Au in an aqueous solution at room temperature for 12 h, the thickness of the Ga oxide layer grows and further hydrolyzes into rod-like GaOOH (Figure 3a). The HAADF image and EDS maps of LM@Au (Figure 3b) indicate that the

Ga oxide layer thickens while the distribution of Ga and In inside remains uniform. To enhance the chemical and colloidal stabilities of the LMNPs and suppress the Ga oxide growth, it has been demonstrated that phosphate salts, such as NaH_2PO_4 , are effective passivation agents.^[19–20] Therefore, we used NaH_2PO_4 to treat LM@Au to prevent the growth of the oxide layer and hydrolysis (Figure 3c). No obvious shape transformation or changes in the oxide layer thickness are observed in the HAADF and EDS maps of the NaH_2PO_4 passivated LM@Au (Figure 3d). Moreover, the EDS spectra (Figure 3e) show that untreated LM@Au has a distinct decrease in the mass ratio of Ga compared with the passivated one, while In remains at a similar mass ratio, verifying that Ga is sacrificed to form the oxide layer. The Ga^{3+} is dissolved into the solution. Due to the higher reduction potential compared with Ga (potentials of $\text{Ga}^{3+}/\text{Ga}^0$, and $\text{In}^{3+}/\text{In}^0$ are -0.529 , and -0.340 V, respectively), In remains unreacted

before the total consumption of Ga.^[12] The XPS survey spectrum obtained for the passivated LM@Au (Figure 3f) detects the peak of P 2p (134.0 eV), indicating the presence of phosphate on the LM@Au surface. The high-resolution O 1s spectrum of untreated LM@Au (Figure S5a, Supporting Information) can be deconvoluted into two peaks (530.9 and 532.0 eV), likely corresponding to Ga—O bond and hydroxyl oxygen (—OH).^[21] Conversely, only one peak at 531.5 eV in the passivated LM@Au is detected, indicating that phosphate groups can effectively prevent oxidation and hydrolyzation.

By adding phosphate at specific time points, it is possible to adjust the thickness of the Ga oxide layer and the size of the coating AuNPs in LM@Au nanostructures. In this study, we added 10 μL of NaH_2PO_4 (10 mM) solution into separate groups of LM@Au suspension (1 mL) at different time points after the galvanic reaction. After 12 h of storage, the samples were observed by TEM (Figure 3g; see Figure S5b, Supporting Information, for details) and optical images (Figure S5c, Supporting Information). The addition of NaH_2PO_4 at different time points has a significant impact on the Ga oxide layer thickness and the diameter of AuNPs in LM@Au. Specifically, as the addition of NaH_2PO_4 is delayed, the Ga oxide layer thickness increases, with the thickness at 12 h being approximately six times thicker than that at 10 s. On the other hand, the diameter of AuNPs decreases and reaches a relatively constant value after 3 min of galvanic reaction (Figure 3h). Importantly, the number of AuNPs on the LM@Au surface increases as the NaH_2PO_4 addition is delayed and gradually stabilizes after 3 min (Figure S5d, Supporting Information). These findings suggest that phosphate groups effectively hinder the oxidation of Ga and compete with AuCl_4^- for surface sites. By occupying the surface sites, the phosphate groups limit the availability of reaction sites for the reduction of AuCl_4^- , thus impeding the further growth of AuNPs.

The presence of AuNPs is reflected in the UV–vis spectra, where the appearance of an Au peak is observed (Figure 3i). With the delay of the addition of NaH_2PO_4 , a red shift in the UV–vis spectra can be noticed. Notably, the LM@Au sample stored for 12 h exhibits a sharp drop in absorbance compared to the other samples. Additionally, the optical image of the 12-h sample appears nearly transparent, indicating that the increased thickness of the Ga oxide layer reduces the suspension's absorbance. Furthermore, when comparing the HAADF image, TEM maps, and EDS spectrum of LM@Au directly obtained after 3 min of galvanic replacement (Figure S5e,f, Supporting Information), no distinct differences are observed when compared to that of LM@Au treated with NaH_2PO_4 at 3 min and stored for 12 h. This observation further confirms that phosphate groups effectively inhibit the growth of the oxide layer, thereby preserving the optical properties of the suspension. Other impact parameters including the concentration of CTAB, HAuCl_4 , and the reaction temperature on the LM@Au morphology, composition, and optical properties are investigated, as given in Figures S6, S7, and Note S1 (Supporting Information).

4. Tuning the Core–Shell Nanostructures

In addition to LM@Au, Au@Ga oxide nanostructures, and hollow Ga oxide can be obtained by simply adjusting the timing of adding HAuCl_4 . To achieve Au@Ga oxide nanostructures, we

first let the Ga oxide layer of the produced LM@Au grow for 12 h and then added an extra 100 μL of HAuCl_4 (100 μM , final concentration of HAuCl_4 is 200 μM) into the suspension. After an additional 12 h of reaction, the inner In-rich core can react with HAuCl_4 . We observed from the TEM image (Figure S8, Supporting Information) obtained earlier than an additional 12 h that Au NPs on the surface of LM displayed the tendency to coalescence. Therefore, we assumed that the newly generated Au NPs and Au NPs on the surface of LM@Au gradually coalesce to form a single Au NP, which is finally covered by a Ga oxide layer, resulting in the formation of Au@Ga oxide nanostructure (Figure 4a). The TEM image (Figure 4b), HAADF image, and EDS maps (Figure 4c) verify the Au@Ga oxide nanostructure. It is important to note that the In element in Au@Ga oxide reduces to a very low level (mass ratio $\approx 2.5\%$), indicating the occurrence of the galvanic replacement between the In-rich core and HAuCl_4 .

The hollow Ga oxide nanostructure was obtained by directly adding an extra 100 μL of HAuCl_4 (100 μM , final concentration of 200 μM) into LM@Au suspension and allowing it to react for 24 h. During this process, HAuCl_4 gradually consumes Ga and In in the LM core, producing large AuNPs and forming the hollow Ga oxide nanostructure (Figure 4d). The TEM image (Figure 4e), HAADF image, and EDS maps (Figure 4f) verify the hollow Ga oxide nanostructure. The XPS spectra of Au@Ga oxide and hollow Ga oxide (Figure S9a, Supporting Information) detect similar peaks of Ga 2p, In 3d, Na 1s, O 1s, and Au 4f. The high-resolution XPS spectrum for the Au 4f peak of Au@Ga oxide (Figure 4g) can be deconvoluted into four peaks, while two peaks are observed for that of hollow Ga oxide & AuNPs. In addition, the high-resolution XPS spectrum for the O 1s peak of Au@Ga oxide has a negative shift compared to that of hollow Ga oxide & AuNPs (Figure S9b, Supporting Information), suggesting the complete oxidation for the hollow Ga oxide nanostructure. The complete oxidation is further verified by comparing the XRD spectra, FTIR spectra, and zeta potential of Au@Ga oxide and hollow Ga oxide & Au NPs (see Figure S9c–e, Supporting Information).

Different core–shell nanostructures exhibit distinct mechanical properties. Using atomic force microscopy (AFM), we measured Young's moduli based on the Hertzian contact model for the produced nanostructures, including LM@Au, hollow Ga oxide, Au@Ga oxide, and LMNP (Figure 4h). Among them, LMNP exhibits the lowest stiffness, with Young's modulus of 125.3 kPa. On the other hand, LM@Au is the hardest, with Young's modulus of 625.63 kPa. This finding suggests that the presence of AuNPs on the surface contributes to increased stiffness. Furthermore, in comparison to hollow Ga oxide, Au@Ga oxide exhibits a higher Young's modulus due to the presence of the Au core.

5. Photothermal Properties of LM@Au

Among the various core–shell nanostructures produced, LM@Au demonstrates a superior photothermal effect (Figure 5a). Under 808 nm laser irradiation (1.0 W cm^{-2}) for a consistent duration of 10 min, we observe the temperature increase for suspensions of AuNPs (see Figure S10a,b, Supporting Information, for the characterization details), LMNPs, Au+LMNPs (directly mix AuNPs with LMNPs), and LM@Au treated by NaH_2PO_4 (NaH_2PO_4 added at different time points: 10 s, 3 min, and 12 h after the galvanic reaction; see Figure S10c,

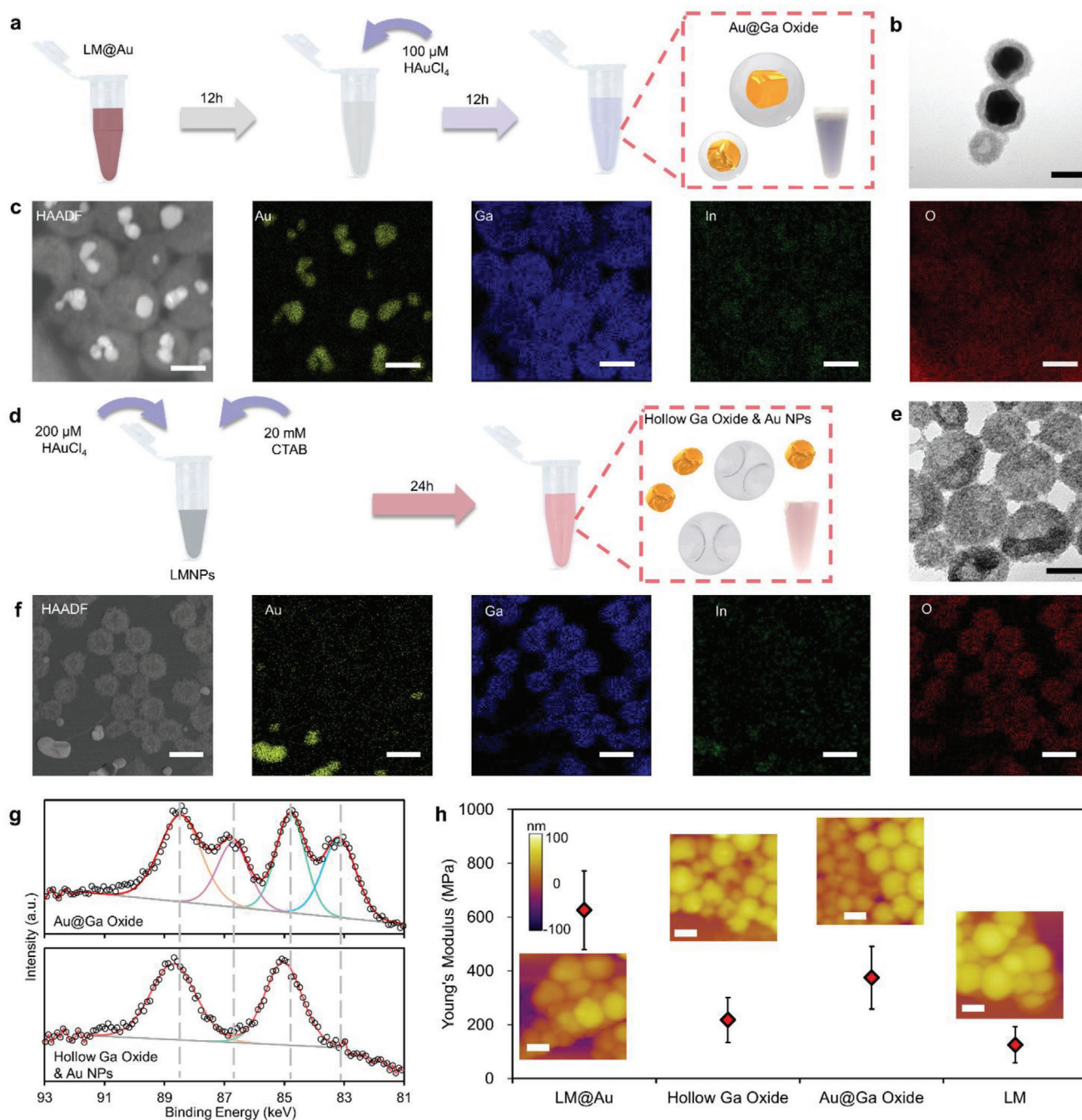


Figure 4. Tuning the core-shell nanostructures. a) Process for producing Au@Ga oxide nanostructures. The inset is the optical image of its suspension. b) TEM image of Au@Ga oxide. The scale bar is 50 nm. c) HAADF images and EDS elemental maps of Au, Ga, In, and O for Au@Ga oxide. Scale bars are 50 nm. d) Process for producing hollow Ga oxide. The inset is the optical image of its suspension. e) TEM image of hollow Ga oxide with separated AuNPs. The scale bar is 50 nm. f) HAADF images and EDS elemental maps of Au, Ga, In, and O for hollow Ga oxide. Scale bars are 50 nm. g) High-resolution XPS spectra for Au 4f signal of both nanostructures. h) Young's moduli and AFM profiles of different core-shell nanostructures. Scale bars are 100 nm.

Supporting Information, for other groups). Interestingly, the temperature of LM@Au is higher compared to Au+LMNPs (see Figure S10d, Supporting Information, for TEM image), indicating an enhanced synergistic effect when AuNPs are attached to the surface of LMNPs. The LM@Au suspension

treated with NaH_2PO_4 after 3 min of the galvanic reaction (LM@Au_{3min}) has the best photothermal effect compared to other groups. We attribute this to the uniform distribution of similarly-sized AuNPs on the LM surface, which enhances light absorption.

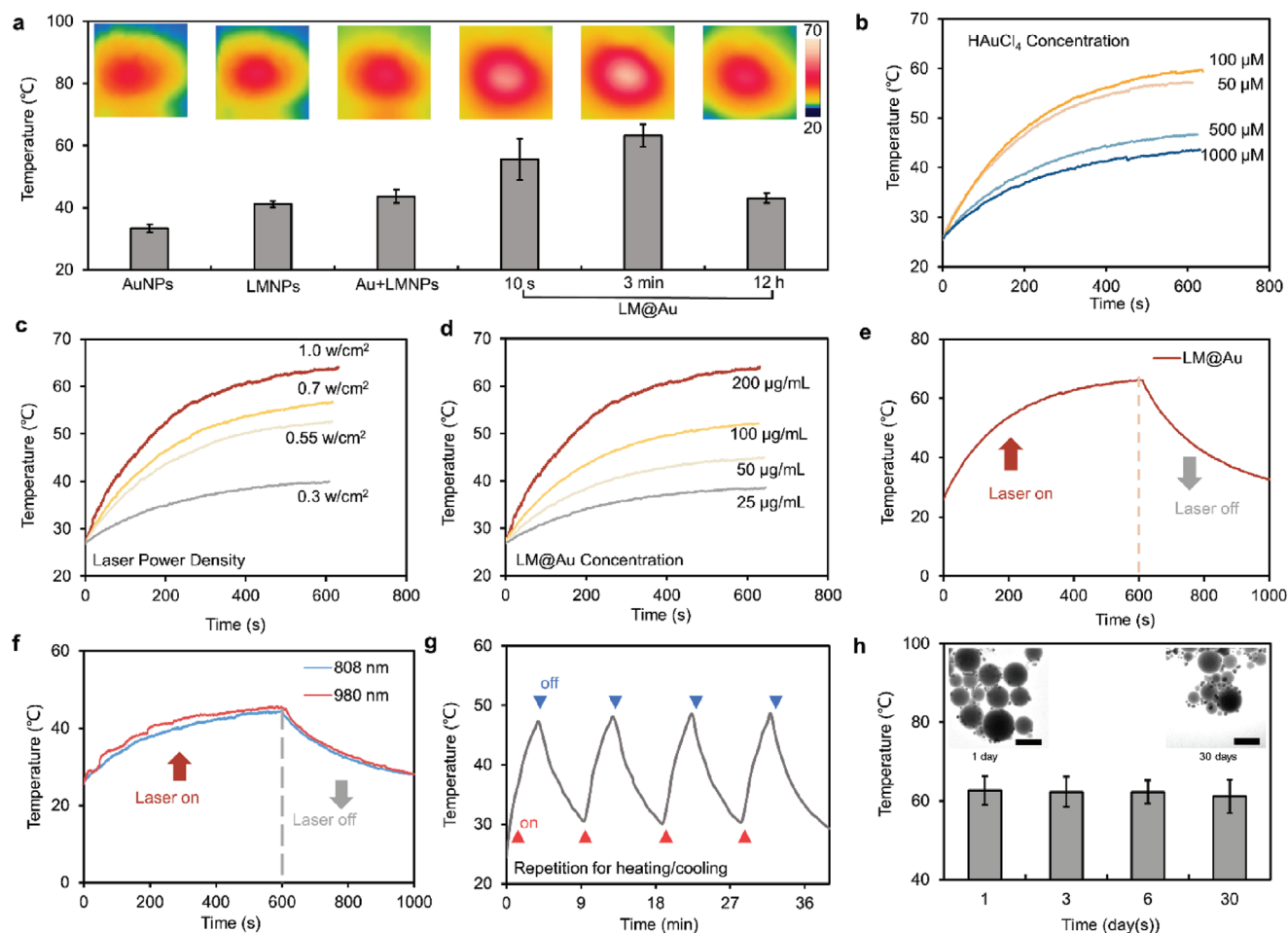


Figure 5. Photothermal properties of LM@Au. a) Ultimate temperature of suspensions of AuNPs, LMNPs, Au+LMNPs, and LM@Au exposed to an 808 nm laser after 10 min. The insets are infrared thermal images of these suspensions at 10 min. b) Photothermal heating curves for LM@Au suspensions prepared with different HAuCl₄ concentrations. c) Photothermal heating curves for LM@Au under 808 nm laser irradiation with different power densities. d) Photothermal heating curves for LM@Au with different concentrations. e) Temperature-time curves of LM@Au (200 μg mL⁻¹) under 808 nm laser irradiation for 600 s followed by 400 s of cooling. f) Temperature variations of LM@Au (50 μg mL⁻¹) under 808 and 980 nm laser irradiation for 600 s followed by 400 s of cooling. g) Temperature variations of LM@Au (200 μg mL⁻¹) for 4 cycles under 808 nm laser irradiation for 4 min followed by 5.4 min of cooling. h) Ultimate temperature of LM@Au_{3min} (after stored for 1, 3, 6, and 30 d) exposed to 808 nm laser irradiation for 10 min. The insets are TEM images for LM@Au 1 and 30 days after production.

In addition, we observe the temperature increase for the suspensions prepared with different HAuCl₄ concentrations (Figure 5b). Notably, the suspension prepared with 100 μM HAuCl₄ generates the highest temperature rise under laser irradiation. This can be attributed to the fact that the sample prepared with 100 μM HAuCl₄ has a greater coating of AuNPs on its surface compared to the sample prepared with 50 μM HAuCl₄. Conversely, suspensions prepared with concentrations exceeding 500 μM tend to excessively consume Ga, leading to the breakdown of the LM@Au nanostructure and degradation of the photothermal effect. Moreover, we observe a positive correlation between the photothermal effect and both laser power density (Figure 5c) and the concentration of LM@Au (Figure 5d), indicating that the temperature increase can be controlled and adjusted.

To characterize the photothermal conversion efficiency (η) of LM@Au_{3min}, we performed temperature measurements on a 300 μL suspension exposed to an 808 nm laser for 600 s. Sub-

sequently, we removed the laser and continued monitoring the temperature for an additional 400 s (Figure 5e). Remarkably, LM@Au_{3min} exhibits an exceptionally high η of 65.9% (see Figure S10e–h and Table S1, Supporting Information, for comparison with other nanomaterials, and Note S2, Supporting Information, for detailed calculation), which is approximately twice as high as that of LMNPs (34.3%). Interestingly, LM@Au_{3min} exposed to lasers with different wavelengths (808 and 980 nm) with the same power density has similar temperature variations (Figure 5f), indicating that the laser wavelength has a negligible impact on the increase of temperature.

To showcase the photothermal stability of LM@Au_{3min}, we conducted temperature measurements for four cycles. Each cycle involved exposing the sample to 808 nm laser irradiation for 4 min, followed by a period of natural cooling for 5.4 min (Figure 5g). No decrease in the peak of temperature is observed. The TEM image for LM@Au_{3min} after undergoing repeated

treatments (Figure S10i, Supporting Information) exhibits a similar morphology to that of the untreated sample, thereby demonstrating the stability of LM@Au_{3min}. However, it is important to note that when the temperature reaches 70 °C under laser irradiation, LM@Au_{3min} may transform into GaOOH (Figure S10j, Supporting Information), which is consistent with previous reports.^[22] Moreover, the stability of LM@Au_{3min} is further confirmed by its ability to retain the initial morphology and exhibit similar photothermal performance even after being stored in an aqueous solution for 30 days (Figure 5h; Figure S10k,l, Supporting Information). This underscores the long-term stability of LM@Au_{3min}.

6. Demonstration of Photothermal Therapy Effect of LM@Au

Given the remarkable photothermal conversion efficiency and chemical stability of LM@Au_{3min}, we conducted further investigations into its potential for photothermal therapy (Figure 6a). First, LM@Au_{3min} was added to cell cultures along with the culture medium, followed by a 24-h incubation period to allow the cells to take in LM@Au_{3min}. Next, laser irradiation was applied to induce the generation of reactive oxygen species (ROS), which promotes cell death. Noticeably, achieving a tumor-killing effect requires the temperature to be kept between 40 and 44 °C, due to the characteristic difference in physiology between normal and tumor cells.^[23] The temperature was kept between 40 and 44 °C during laser irradiation. After an additional 24-h incubation, these cells undergo apoptosis.

To demonstrate the effectiveness of photothermal therapy, we evaluated the cell viabilities of different tumor cell lines (4T1, D425, and SHSY5Y) treated with LM@Au_{3min} with/without laser irradiation (Figure 6b; Figure S11a,b, and Table S1, Supporting Information, for comparison with other nanomaterials). It is worth noting that the reactive Ga is easily affected by the pH of the solution, allowing for the leaching of Ga ions in the biological buffer and even after the photothermal process.^[24] The ferro-similar properties of Ga ions may interfere with the iron-dependent cellular function of cells.^[25] The cell viability without laser irradiation is consistently higher than 80%, indicating low cytotoxicity and excellent biocompatibility of LM@Au_{3min}. Upon laser irradiation, the cell viability sharply decreases as the concentration of LM@Au_{3min} increases. At a concentration of 20 μg mL⁻¹ LM@Au_{3min}, the cell survival ratio is lower than 50%. The photothermal performance of LM@Au_{3min} is effectively enhanced by increasing the duration of laser irradiation (Figure 6c; Figure S11c, Supporting Information) or the power density of the laser (Figure 6d; Figure S11d, Supporting Information).

Moreover, confocal fluorescence images of 4T1 cells with/without laser irradiation are obtained (Figure 6e). The live cells are labeled with Calcein AM (green), while the dead cells are labeled with Ethidium Homodimer-1 (red). In the absence of LM@Au_{3min} or laser irradiation, the majority of 4T1 cells remain viable. In contrast, a distinct red signal is observed in the group treated with LM@Au_{3min} and subjected to laser irradiation, confirming the excellent photothermal therapeutic effect. We hypothesize that hyperthermia induced by LM@Au_{3min} causes the generation of ROS (including superoxide, hydrogen peroxide, and hydroxyl radicals), leading to

cell death.^[26] The levels of ROS are significantly higher in the group treated with LM@Au_{3min} and laser irradiation compared to the groups without LM@Au_{3min} or laser irradiation (Figure 6f; Figure S11e,f, Supporting Information), thus verifying the role of ROS in the process of cell death.

7. Conclusion

In this study, we develop a straightforward nanoengineering strategy for creating diverse LM core-shell nanostructures through galvanic replacement. LM@Au nanostructures with evenly distributed, similarly sized AuNP coating are successfully fabricated by adding HAuCl₄ and CTAB to the LMNP solution. The presence of NaH₂PO₄ can precisely control the morphology of LM@Au and the size of the coated AuNPs. It achieves this by inhibiting the growth of the Ga oxide layer and preventing galvanic replacement. Notably, adjusting the chemical concentration and the timing of addition enables the formation of unprecedented Au@Ga oxide and hollow Ga oxide nanostructures. These nanostructures exhibit different Young's moduli, reflecting the impact of their unique compositions on their mechanical properties. Remarkably, LM@Au exhibits a significantly enhanced synergetic effect for photothermal performance, surpassing that of AuNPs, LMNPs, and the mixture of AuNPs and LMNPs. LM@Au_{3min} shows the highest photothermal conversion efficiency of 65.9%, which is five times that of AuNPs conventionally used for biomedicine. In addition, NaH₂PO₄-treated LM@Au_{3min} has superior photothermal stability (below 50 °C) and maintains its original structure and excellent photothermal conversion efficiency in biological buffers for over 30 days without degradation. Upon laser irradiation, LM@Au_{3min} exhibits rapid and efficient heat generation within tumor cells. This localized hyperthermia leads to the generation of ROS and subsequent cell death. This remarkable capability further reinforces the superiority of LM@Au in terms of photothermal efficiency and underscores its unique advantages for therapeutic applications. We believe that our strategy for creating tunable core-shell nanostructures holds great promise in facilitating the on-demand production of innovative nanostructures. This approach is not limited to biomedicine alone but extends its potential to advance numerous other fields.

8. Experimental Section

Materials: Eutectic gallium indium (EGaIn), Chloroauric acid, hexadecyltrimethylammonium bromide (CTAB), 2,2'-azobis(2-methylpropionitrile) (AIBN), chloroauric acid (HAuCl₄), sodium dihydrogen phosphate (NaH₂PO₄), ethylene glycol methyl ether methacrylate (EGMA), 4-Cyano-4-((ethylthio)carbonothioyl)thio)pentanoic acid (CEPA), sodium dihydrogen phosphate calcein-AM, and ethidium homodimer (EthD-1) were purchased from Sigma-Aldrich, Australia. RPMI 1640 medium, fetal bovine serum (FBS), Dulbecco's Modified Eagle Medium F12 (DMEM F12), and Minimum Essential Medium (MEM) were purchased from Gibco, Thermo Fisher Scientific, Australia. 2,7-Dichlorofluorescein Diacetate (DCFDA) – cellular ROS assay kit was purchased from Abcam, UK. AlamarBlue was purchased from Bio-Rad, Australia.

Characterizations: Transmission electron microscopy (TEM) images and EDS spectra were obtained using Hitachi HT 7700. TEM maps were obtained using a transmission electron microscope HF5000. The

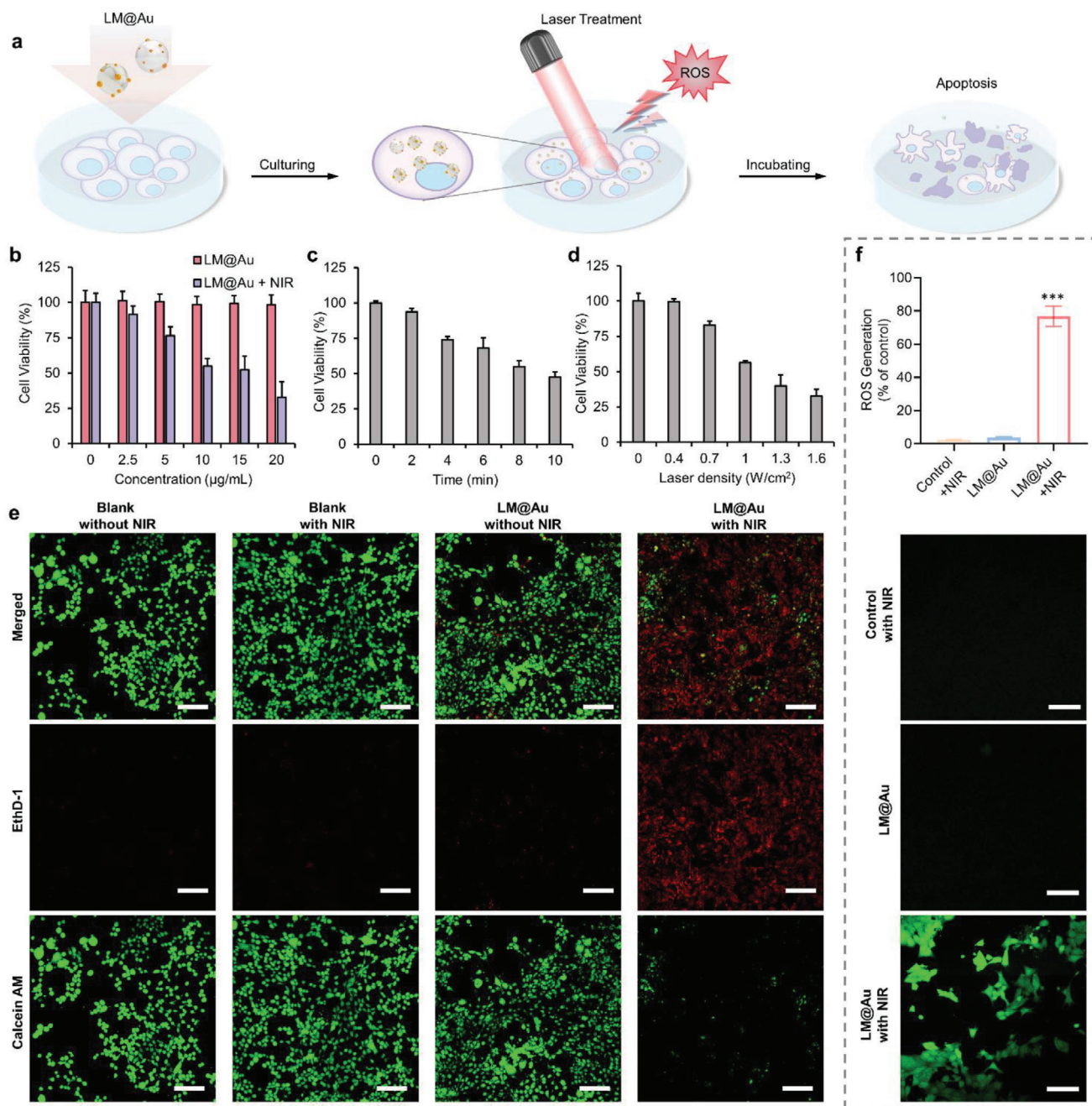


Figure 6. Photothermal therapy of LM@Au_{3min}. a) Schematic showing the photothermal therapy process using LM@Au_{3min}. b) Cell viability of 4T1 cells containing different concentrations of LM@Au_{3min} with/without 808 nm laser irradiation (1.0 W cm⁻²). c) Cell viability of 4T1 cells containing LM@Au_{3min} after 808 nm laser irradiation (1.0 W cm⁻²) for different periods. d) Cell viability of 4T1 cells containing LM@Au_{3min} under 808 nm laser irradiation with different power densities. e) Confocal fluorescence images of 4T1 cells with/without the addition of LM@Au_{3min} after 808 nm laser irradiation. The cells are stained with calcein AM (green, live cells) and Ethidium Homodimer-1 (EthD-1) (red, dead cells). f) ROS generation for 4T1 cells with/without LM@Au_{3min} after 808 nm laser irradiation.

hydrodynamic distributions of NPs were obtained using Zetasizer Advance, Malvern Instrument, Malvern, UK. XPS spectra were obtained using Kratos Axis Ultra XPS, Japan. The UV-vis absorbance spectra were obtained using UV-2600, Shimadzu, Japan. FTIR spectra were obtained using an FTIR Spectrometer (Nicolet 6700). XRD spectra were obtained using powder XRD (Bruker D8 Advance). The Young's moduli of nanostructures

were measured by Cypher atomic force microscope (AFM) (Asylum Research, Santa Barbara, CA, USA). The temperature variations were measured by the FLIR E50 infrared camera (Teledyne FLIR, USA). The viability of cells was obtained by BioTek Plate Reader (Biotek Synergy HT). The fluorescent images were obtained using a Lecia SP8 confocal microscope (Lecia Microsystems, USA).

Synthesis of PEGMA: The process for synthesizing the PEGMA was given in the previous work.^[27] In brief, the reversible addition-fragmentation chain transfer (RAFT) agents of CEPA (126 mg), EGMA (1.2 g), and AIBN (1.6 mg) were dissolved in 1 mL of anhydrous 1, 4-dioxane. Then, the mixture reacted at 70 °C for 4 h under vacuum after three cycles of freeze-pump-thaw. The polymerization was terminated by freezing with liquid nitrogen, and the final product was obtained by precipitating twice in 40 mL of ether and drying.

Preparation of LMNPs: EGaIn (200 mg) and PEGMA (40 mg) were added into a vial containing milliQ water (10 mL) and then sonicated by a sonication probe (VCX 750, Sonics, USA) with a diameter of 3 mm at 20% power intensity for 20 min (45 s on and 15 s off) using the dynamic temperature control system.^[19] After that, the solution was centrifuged (2400 rpm, 4 min) to remove large particles. The supernatant was collected and further centrifuged (10 000 rpm, 10 min, twice) to obtain LMNPs.

Preparation of LM@Au: 100 μL HAuCl_4 (1 mM) and 200 μL CTAB (0.1 M) were mixed vigorously into a 1.5 mL centrifuge tube. Next, LMNPs (200 μg) were added into the tube and then diluted with water up to 1 mL, followed by thorough mixing. 3 min later, the solution was centrifuged (10 000 rpm, 10 min, twice) to obtain LM@Au.

Influence of Phosphate on the Morphology of LM@Au: 100 μL of 1 mM HAuCl_4 and 200 μL of 0.1 M CTAB were vigorously mixed in a 1.5 mL centrifuge tube. Next, 200 μg of LMNPs were added to the tube and diluted with milliQ water up to 1 mL, followed by thorough mixing. This process was repeated ten times to prepare ten solutions. One of the solutions was directly centrifuged twice (at 10 000 rpm for 10 min) after 3 min of mixing to obtain the final product. For the remaining solutions, 10 μL of 10 mM NaH_2PO_4 aqueous solution was added at different intervals, starting from 10 s and up to 12 h. After 12 h, these solutions were centrifuged twice (at 10 000 rpm for 10 min) to obtain the final product.

Influence of the Concentration of CTAB on LM@Au: 100 μL HAuCl_4 (1 mM) and 2/20/200 μL CTAB (10 mM) were mixed vigorously in a 1.5 mL centrifuge tube. Next, LMNPs (200 μg) were added to the tube and then diluted with milliQ water up to 1 mL, followed by thorough mixing. 10 μL NaH_2PO_4 aqueous solution (10 mM) was added into these final solutions after 3 min. After 12 h, the solutions were centrifuged (10 000 rpm, 10 min, twice) to obtain the final product.

Influence of the Concentration of HAuCl_4 and Reaction Temperature on LM@Au: 100 μL HAuCl_4 (0.5/1/5/10 mM) and 200 μL CTAB (0.1 M) were mixed vigorously in a 1.5 mL centrifuge tube. Next, LMNPs (200 μg) were added to the tube and then diluted with milliQ water up to 1 mL, followed by thorough mixing at room temperature. 10 μL NaH_2PO_4 aqueous solution (10 mM) was added into these final solutions after 3 min. In the meantime, solutions without adding 10 μL NaH_2PO_4 aqueous solution (10 mM) were also prepared following the same process. After 12 h, the solutions were centrifuged (10 000 rpm, 10 min, twice) to obtain the final product. Besides, those entire processes were also carried out in an ice batch and 60 °C.

Preparation of Au@Ga Oxide: 100 μL HAuCl_4 (1 mM) and 200 μL CTAB (0.1 M) were mixed vigorously in a 1.5 mL centrifuge tube. Next, LMNPs (200 μg) were added to the tube and then diluted with milliQ water up to 900 μL , followed by thorough mixing. After 12 h, an additional 100 μL of 1 mM HAuCl_4 was added to the suspension. Another 12 h later, the solution was centrifuged (10 000 rpm, 10 min, twice) to obtain Au@Ga oxide.

Preparation of Hollow Ga Oxide: 200 μL HAuCl_4 (1 mM) and 200 μL CTAB (0.1 M) were mixed vigorously in a 1.5 mL centrifuge tube. Next, LMNPs (200 μg) were added to the tube and then diluted with milliQ water up to 1 mL, followed by thorough mixing. After 24 h, the solution was centrifuged (10 000 rpm, 10 min, twice) to obtain hollow Ga oxide.

Preparation of AuNPs: The HAuCl_4 aqueous solution (0.25 mM) was heated to 100 °C for 10 min, followed by the addition of sodium citrate (1.7 mM). The reaction was allowed to continue until the solution color turned red, after which the solution was cooled down to room temperature.

In Vitro Photothermal Performance: The suspensions mentioned above (300 μL) in a 96-well plate were irradiated by an 808 nm laser (1.0 W cm^{-2}) for 10 min and naturally cooled down for 400 s. To investi-

gate the influence of the power density, LM@Au was fixed at 200 $\mu\text{g mL}^{-1}$ and then irradiated by 808 nm laser with the power density of 0.3, 0.55, 0.7, and 1.0 W cm^{-2} . In addition, the laser with different wavelengths (880 and 980 nm) was applied to LM@Au with the same process to investigate the impact of laser wavelength. As for the photothermal stability, LM@Au was exposed to an 808 nm laser for 4 min followed by natural cooling for 5.4 min with 4 cycles. To demonstrate the stability, LM@Au stored for 1/3/6/30 days was irradiated by an 808 nm laser (1.0 W cm^{-2}) for 10 min.

Cell Culture: 4T1 (4T1 – CRL-2539-ATCC, USA) cells were incubated in RPMI 1640 medium containing 10% FBS at 37 °C in a humidified atmosphere containing 5% CO_2 . D425 (D425 SCC290-Merk, Australia) cells were incubated in Eagle's minimal essential medium containing 20% FBS at 37 °C in a humidified atmosphere containing 5% CO_2 . SHSY5Y (SHSY5Y – CRL-2266-ATCC, USA) cells were incubated in DMEM F12 medium containing 10% FBS at 37 °C in a humidified atmosphere containing 5% CO_2 .

In Vitro Cytotoxicity: The alamarBlue assay was used to investigate the cytotoxicity of LM@Au at various concentrations, following exposure to laser with different irradiation times and power densities in 4T1/D425/SHSY5Y cells. The cells were seeded in 96-well plates at a density of 10 000 cells per well in 100 μL of media and incubated for 24 h. After that, LM@Au was added into the wells, followed by co-incubation for 6 h. Subsequently, the cells were exposed to an 808 nm laser with different power densities and irradiation times. The alamarBlue assay was performed to determine cell viability.

Live/Dead Cell Staining Assay: To investigate the cell status after laser irradiation, 4T1 cells were seeded in 8-well plates at a density of 20 000 cells per well for 24 h. LM@Au_{3min} were added into cells to further co-incubate for 6 h and then cells (including that nothing added) were irradiated by 808 nm laser (1.6 W cm^{-2}) for 10 min. After 24 h incubation, these cells were incubated with calcein-AM (2 μM) and ethidium homodimer (EthD-1) (4 μM) in PBS buffer solution at 37 °C for 30 min. After that, the cells were washed with PBS 3 times and observed by a confocal microscope.

Ros Generation Assay: 4T1 cells were seeded in 8-well plates at a density of 20 000 cells per well and incubated for 24 h. LM@Au was added to the cells and co-incubated for 6 h, after which the cells (including the control group without LM@Au) were irradiated with an 808 nm laser (1.6 W cm^{-2}) for 10 min. After a 4-h incubation, the cells were treated with 2,7-Dichlorofluorescein Diacetate (DCFDA) at 37 °C for 30 min and observed using a confocal microscope.

Supporting Information

Supporting Information is available from the Wiley Online Library or from the author.

Acknowledgements

R.Q. gratefully acknowledges the research funded by the National Health and Medical Research Council (APP1196850). This work used the Queensland node of the NCRIS-enabled Australian National Fabrication Facility (ANFF) and the Centre for Microscopy and Microanalysis (CMM). S.-Y.T. gratefully acknowledges the research funded by the Engineering and Physical Sciences Research Council (EPSRC) grant (EP/V008382/1). W.L. gratefully acknowledges the research funded by the Australian Research Council (DP230100823).

Open access publishing facilitated by The University of Queensland, as part of the Wiley - The University of Queensland agreement via the Council of Australian University Librarians.

Conflict of Interest

The authors declare no conflict of interest.

Data Availability Statement

The data that support the findings of this study are available in the supplementary material of this article.

Keywords

core–shell nanostructures, galvanic replacement, liquid metals, photothermal conversion efficiency

Received: September 18, 2023
Revised: October 10, 2023
Published online:

- [1] a) F. Caruso, *Adv. Mater.* **2001**, *13*, 11; b) S. Zhao, Z. Guo, J. Yang, C. Wang, B. Sun, G. Wang, *Small* **2021**, *17*, 2007431; c) S. Rahman, Y. Lu, *Nanoscale Horiz.* **2022**, *7*, 849; d) X. Jing, Y. Zhang, M. Li, X. Zuo, C. Fan, J. Zheng, *Mater. Horiz.* **2023**, *10*, 1185.
- [2] a) Y. Mao, T.-J. Park, F. Zhang, H. Zhou, S. S. Wong, *Small* **2007**, *3*, 1122; b) C. Jia, Z. Lin, Y. Huang, X. Duan, *Chem. Rev.* **2019**, *119*, 9074; c) D. Wan, X. Xia, Y. Wang, Y. Xia, *Small* **2013**, *9*, 3111; d) Q. Li, Y. Cui, J. Lin, C. Zhao, L. Ding, *J. Ind. Eng. Chem.* **2022**, *110*, 542.
- [3] J. Gim, A. Koch, L. M. Otter, B. H. Savitzky, S. Erland, L. A. Estroff, D. E. Jacob, R. Hovden, *Proc. Natl. Acad. Sci. USA* **2021**, *118*, e2107477118.
- [4] a) Y. Zhong, Z. Ma, F. Wang, X. Wang, Y. Yang, Y. Liu, X. Zhao, J. Li, H. Du, M. Zhang, Q. Cui, S. Zhu, Q. Sun, H. Wan, Y. Tian, Q. Liu, W. Wang, K. C. Garcia, H. Dai, *Nat. Biotechnol.* **2019**, *37*, 1322; b) Z. Gao, Y. Hou, J. Zeng, L. Chen, C. Liu, W. Yang, M. Gao, *Adv. Mater.* **2017**, *29*, 1701095.
- [5] J. Zhang, D. Cheng, J. He, J. Hong, C. Yuan, M. Liang, *Nat. Protoc.* **2021**, *16*, 4878.
- [6] Y. Chao, P. Zhou, J. Lai, W. Zhang, H. Yang, S. Lu, H. Chen, K. Yin, M. Li, L. Tao, C. Shang, M. Tong, S. Guo, *Adv. Funct. Mater.* **2021**, *31*, 2100923.
- [7] a) P. Mahajan, A. Singh, S. Arya, *J. Alloys Compd.* **2020**, *814*, 152292; b) J. Cao, B. Wang, D. Han, S. Yang, Q. Liu, T. Wang, H. Niu, J. Yang, *Mater. Lett.* **2014**, *135*, 71; c) H. T. Maune, S.-p. Han, R. D. Barish, M. Bockrath, W. A. G. Iii, P. W. K. Rothmund, E. Winfree, *Nat. Nanotechnol.* **2010**, *5*, 61; d) M. Schroffenegger, N. S. Leitner, G. Morgese, S. N. Ramakrishna, M. Willinger, E. M. Benetti, E. Reimhult, *ACS Nano* **2020**, *14*, 12708.
- [8] a) X. Xia, Y. Wang, A. Ruditskiy, Y. Xia, *Adv. Mater.* **2013**, *25*, 6313; b) S. W. Chee, S. F. Tan, Z. Baraissov, M. Bosman, U. Mirsaidov, *Nat. Commun.* **2017**, *8*, 1224.
- [9] a) L. Zheng, S. Handschuh-Wang, Z. Ye, B. Wang, *Appl. Mater. Today* **2022**, *27*, 101423; b) F.-M. Allieux, M. B. Ghasemian, W. Xie, A. P. O'Mullane, T. Daeneke, M. D. Dickey, K. Kalantar-Zadeh, *Nanoscale Horiz.* **2022**, *7*, 141; c) K. Y. Kwon, V. K. Truong, F. Krisnadi, S. Im, J. Ma, N. Mehrabian, T.-I. Kim, M. D. Dickey, *Advanced Intelligent Systems* **2021**, *3*, 2000159; d) H. Li, R. Qiao, T. P. Davis, S.-Y. Tang, *Biosensors* **2020**, *10*, 196; e) W. Gao, Y. Wang, Q. Wang, G. Ma, J. Liu, *J. Mater. Chem. B* **2022**, *10*, 829; f) C. Zhang, B. Yang, J. M. Biazik, R. F. Webster, W. Xie, J. Tang, F.-M. Allieux, R. Abbasi, M. Mousavi, E. M. Goldys, K. A. Kilian, R. Chandrawati, D. Esraflzadeh, K. Kalantar-Zadeh, *ACS Nano* **2022**, *16*, 8891; g) F. Centurion, R. Namivandi-Zangeneh, N. Flores, M. Tajik, S. Merhebi, R. Abbasi, M. Mayyas, F.-M. Allieux, J. Tang, W. A. Donald, C. Boyer, M. D. Dickey, K. Kalantar-Zadeh, M. d. A. Rahim, *ACS Appl. Nano Mater.* **2021**, *4*, 2987.
- [10] a) S. Y. Tang, R. Qiao, S. Yan, D. Yuan, Q. Zhao, G. Yun, T. P. Davis, W. Li, *Small* **2018**, *14*, 1800118; b) S.-Y. Tang, R. Qiao, Y. Lin, Y. Li, Q. Zhao, D. Yuan, G. Yun, J. Guo, M. D. Dickey, T. J. Huang, T. P. Davis, K. Kalantar-Zadeh, W. Li, *Adv. Mater. Technol.* **2019**, *4*, 1800420; c) I. D. Tevis, L. B. Newcomb, M. Thuo, *Langmuir* **2014**, *30*, 14308; d) F. Yu, J. Xu, H. Li, Z. Wang, L. Sun, T. Deng, P. Tao, Q. Liang, *Prog. Nat. Sci.: Mater. Int.* **2018**, *28*, 28.
- [11] a) Y. Lin, J. Genzer, W. Li, R. Qiao, M. D. Dickey, S.-Y. Tang, *Nanoscale* **2018**, *10*, 19871; b) H. Bark, P. S. Lee, *Chem. Sci.* **2021**, *12*, 2760; c) S.-Y. Tang, C. Tabor, K. Kalantar-Zadeh, M. D. Dickey, *Ann. Rev. Mater. Res.* **2021**, *51*, 381.
- [12] a) L. Castilla-Amorós, D. Stoian, J. R. Pankhurst, S. B. Varandili, R. Buonsanti, *J. Am. Chem. Soc.* **2020**, *142*, 19283; b) F. Hoshyargar, J. Crawford, A. P. O'mullane, *J. Am. Chem. Soc.* **2017**, *139*, 1464.
- [13] a) M. B. Ghasemian, M. Mayyas, S. A. Idrus-Saidi, M. A. Jamal, J. Yang, S. S. Mofarah, E. Adabifiroozjaei, J. Tang, N. Syed, A. P. O'Mullane, T. Daeneke, K. Kalantar-Zadeh, *Adv. Funct. Mater.* **2019**, *29*, 1901649; b) O. Oloye, J. F. S. Fernando, E. R. Waclawik, D. Golberg, A. P. O'mullane, *New J. Chem.* **2020**, *44*, 14979.
- [14] a) T. Wang, Y. Zhang, Q. Liu, W. Cheng, X. Wang, L. Pan, B. Xu, H. Xu, *Adv. Funct. Mater.* **2018**, *28*, 1705551; b) R. Zheng, Z. Peng, Y. Fu, Z. Deng, S. Liu, S. Xing, Y. Wu, J. Li, L. Liu, *Adv. Funct. Mater.* **2020**, *30*, 1910524.
- [15] Z. Guo, J. Lu, D. Wang, W. Xie, Y. Chi, J. Xu, N. Takuya, J. Zhang, W. Xu, F. Gao, H. Wu, L. Zhao, *Bioact. Mater.* **2021**, *6*, 602.
- [16] Z. Guo, W. Xie, X. Gao, J. Lu, J. Ye, Y. Li, A. Fahad, G. Zhang, L. Zhao, *Small* **2023**, *19*, 2300751.
- [17] a) Y. Yao, S. Chen, J. Ye, Y. Cui, Z. Deng, *ACS Appl. Mater. Interfaces* **2021**, *13*, 60660; b) R. David, N. Miki, *Langmuir* **2018**, *34*, 10550.
- [18] X. Huang, T. Xu, A. Shen, T. P. Davis, R. Qiao, S.-Y. Tang, *ACS Appl. Nano Mater.* **2022**, *5*, 5959.
- [19] H. Lu, S.-Y. Tang, Z. Dong, D. Liu, Y. Zhang, C. Zhang, G. Yun, Q. Zhao, K. Kalantar-Zadeh, R. Qiao, *ACS Appl. Nano Mater.* **2020**, *3*, 6905.
- [20] J. R. Edwards, *Comput. Fluids* **1997**, *26*, 635.
- [21] T. Gan, S. Handschuh-Wang, W. Shang, X. Zhou, *Langmuir* **2022**, *38*, 14475.
- [22] a) Y. Lin, Y. Liu, J. Genzer, M. D. Dickey, *Chem. Sci.* **2017**, *8*, 3832; b) D. Kim, J. Hwang, Y. Choi, Y. Kwon, J. Jang, S. Yoon, J. Choi, *Cancers* **2019**, *11*, 1666.
- [23] K. Ahmed, Y. Tabuchi, T. Kondo, *Apoptosis* **2015**, *20*, 1411.
- [24] a) L. Mou, J. Qi, L. Tang, R. Dong, Y. Xia, Y. Gao, X. Jiang, *Small* **2020**, *16*, 2005336; b) F. Pourhossein, S. M. Mousavi, F. Beolchini, *Resour. Conserv. Recycle* **2022**, *182*, 106306.
- [25] C. R. Chitambar, *Biochimica et Biophysica Acta (BBA)-Mol. Cell Res.* **2016**, *1863*, 2044.
- [26] Z. Zhou, J. Song, L. Nie, X. Chen, *Chem. Soc. Rev.* **2016**, *45*, 6597.
- [27] X. Ma, X. Shi, S. Bai, Y.-E. Gao, M. Hou, M.-Y. Han, Z. Xu, *J. Mater. Sci.* **2018**, *53*, 892.